POLITECNICO DI TORINO
Repository ISTITUZIONALE

Esterase-Cleavable 2D Assemblies of Magnetic Iron Oxide Nanocubes: Exploiting Enzymatic Polymer Disassembling to Improve Magnetic Hyperthermia Heat Losses

(Article begins on next page)

17 October 2023

Esterase-Cleavable 2D Assemblies of Magnetic Iron Oxide Nanocubes: Exploiting Enzymatic Polymer Disassembling To Improve Magnetic Hyperthermia Heat Losses

Sahitya Kumar Avugadda,[†,‡,¶] Maria Elena Materia,[†,¶] Rinat Nigmatullin,[§] David Cabrera,[∥] Roberto Marotta,[†] Tamara Fernandez Cabada,[†] Elena Marcello,[§] Simone Nitti,[†] Emilio J. Artés-Ibañez,[∥] Pooja Basnett,[§] Claire Wilhelm,[⊥] Francisco J. Teran,[∥,#] Ipsita Roy,[§] and Teresa Pellegrino*,[†]

[†]Istituto Italiano di Tecnologia, via Morego 30, 16163 Genoa, Italy

[‡]Dipartimento di Chimica e Chimica Industriale, Università di Genova, Via Dodecaneso, 31, 16146 Genova, Italy

[§]School of Life Sciences, College of Liberal Arts and Sciences, University of Westminster, New Cavendish Street, London W1W 6UW, U.K.

[∥]iMdea Nanociencia, Campus Universitario de Cantoblanco, C/ Faraday 9, 28049 Madrid, Spain

[⊥]Laboratoire Matière et Systèmes Complexes (MSC) UMR 7057 CNRS and Université Paris Diderot, 75205 Paris Cedex 05, France

[#]Unidad Asociada al Centro Nacional de Biotecnología (CSIC), Nanobiotecnología (iMdea Nanociencia), 28049 Madrid, Spain

S *Supporting Information*
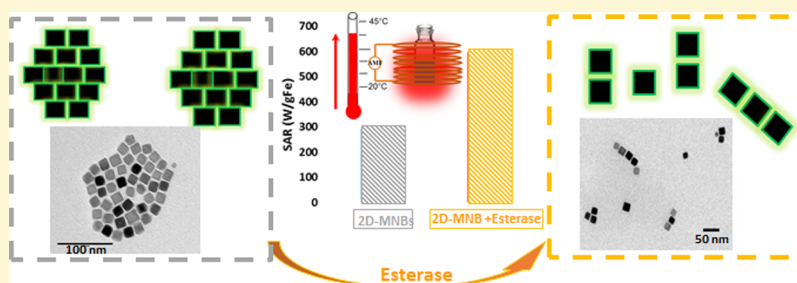
ABSTRACT: Here, we report a nanoplatform based on iron oxide nanocubes (IONCs) coated with a bioresorbable polymer that, upon exposure to lytic enzymes, can be disassembled increasing the heat performances in comparison with the initial clusters. We have developed two-dimensional (2D) clusters by exploiting benchmark IONCs as heat mediators for magnetic hyperthermia and a polyhydroxyalkanoate (PHA) copolymer, a biodegradable polymer produced by bacteria that can be digested by intracellular esterase enzymes. The comparison of magnetic heat performance of the 2D assemblies with 3D centrosymmetrical assemblies or single IONCs emphasizes the benefit of the 2D assembly. Moreover, the heat losses of 2D assemblies dispersed in water are better than the 3D assemblies but worse than for single nanocubes. On the other hand, when the 2D magnetic beads (2D-MNBs) are incubated with the esterase enzyme at a physiological temperature, their magnetic heat performances began to progressively increase. After 2 h of incubation, specific absorption rate values of the 2D assembly double the ones of individually coated nanocubes. Such an increase can be mainly correlated to the splitting of the 2D-MNBs into smaller size clusters with a chain-like configuration containing few nanocubes. Moreover, 2D-MNBs exhibited nonvariable heat performances even after intentionally inducing their aggregation. Magnetophoresis measurements indicate a comparable response of 3D and 2D clusters to external magnets (0.3 T) that is by far faster than that of single nanocubes. This feature is crucial for a physical accumulation of magnetic materials in the presence of magnetic field gradients. This system is the first example of a nanoplatform that, upon exposure to lytic enzymes, such as those present in a tumor environment, can be disassembled from the initial 2D-MNB organization to chain-like assemblies with clear improvement of the heat magnetic losses resulting in better heat dissipation performances. The potential application of 2D nanoassemblies based on the cleavable PHAs for preserving their magnetic losses inside cells will benefit hyperthermia therapies mediated by magnetic nanoparticles under alternating magnetic fields.

INTRODUCTION

Magnetic hyperthermia (MH) is a noninvasive and clinically approved treatment for glioblastoma multiforme, an aggressive brain tumor. It exploits magnetic nanoparticles (MNPs) as

heat agents, and it is now under clinical trial for other solid tumors.[1,2] Using current available MNPs and an alternating magnetic field (AMF) of clinical use (110 kHz in frequency and 15 kA m^{-1} in magnetic field amplitude),[2] a high dose of the magnetic material (usually a 0.5−12 mL of iron oxide solutions at a concentration of 112 mg$_{Fe}$/mL per treatment per patient) needs to be used in order to achieve the desired therapeutic temperature range (42−45 °C). This is mainly due to the poor heat performance of the MNPs that are currently being used in clinic avoiding magnetic dipolar interactions that strongly shrinks their MH efficiency inside cells.[3−5] Injecting such a high dose of MNPs impairs the use of magnetic resonance imaging (MRI), which is commonly used to scan the brain.[6] Substantial efforts have been made to tune the size, shape, crystallinity, and composition of MNPs to achieve outstanding heating performance with a new generation of iron-based nanoparticles.[7,8] Among the MNPs available, iron oxide nanoparticles with cubic morphologies significantly stand out as a result of their specific absorption rate (SAR) values, which have been reported to be 10−20 times higher than those of spherical iron oxide nanoparticles.[9,10] It is also worth mentioning that cubic-shaped MNPs that derive from magnetosome bacteria arranged in chain-like clusters have been reported to possess a better heat performance than that of single particles—according to SAR values[11] for both MH[12,13] and MRI applications.[14] At a mesoscale range, dipolar magnetic interactions in such chain assemblies positively alter the physical interactions of the magnetic dipoles of single nanoparticles and eventually differentiate the magnetic properties from the isolated particles.[15]

Inspired by these chains, many groups have engaged in exploring the effects of clustering MNPs into different morphologies for magnetic fluid hyperthermia.[8,12,16−20] For instance, some groups including the Pellegrino group synthesized colloidally stable short chains (dimer and trimer assemblies) of nanocubes (NCs) and compared their heat performances to those of single NCs or their centrosymmetrical assemblies.[21] The enhancement of the SAR values of these iron oxide NCs (IONCs) (in the form of dimers/trimers) was favored by variations of the effective magnetic anisotropy of the NC chains and the long-range dipolar interactions between the nanocrystals.[22] The long-range dipolar interaction of the particles resulted in a cluster with a chain-like spatial distribution whose magnetic easy axis remains parallel to each crystal and leads to the macroscopic, magnetization moment.[18,20] On the contrary, in 3D assemblies, the closed magnetic moments are arranged in a three-dimensional assembly where nanoparticles have a random spatial distribution, resulting in a decrease of magnetization, and consequently, reduction of heating performance.[19,23] On the other hand, 3D and 2D clusters, being composed of multiple MNPs which can align simultaneously to an external magnet, accumulate much quicker than individual MNPs to an external magnet.[24] The quick response is crucial for magnetically guided MNPs in order to apply local MH or heat-mediated drug delivery at sufficient MNPs dose at the tumor site.

While many methods have been reported for three-dimensional magnetic beads (3D-MNBs),[8,19,25] only few attempts to obtain a 2D assembly of MNPs have been successful: some of them were using solid substrate-based deposition methods such as the Langmuir−Blodgett technique,[26,27] a chemically assisted self-assembly technique,[28] or a magnetic field-induced assembly technique.[29] The as-produced monolayers of MNPs, which are in the micrometer size range, were applied to magnetic storage, sensing, or filtering applications.[30−33] To date, there have been very few reports on colloidally stable 2D assemblies of inorganic nanoparticles, but one example of such work is that of Yan et al. on self-assembling Au NPs into 2D nanogrids, using DNA as a mediator for nano-optonic applications.[34] Andreu et al. have also reported a magnetic study on a micrometer 2D assembly of MNPs in an epoxy resin solid matrix or on a 2D arrangement of groups of a few nanoparticles (from 2 to 12) when they are embedded in a PLGA nanosphere that is 200 nm in size. Although this paper has pioneered the work on NC arrangements in hyperthermia, because of the choice of the initial particles with poor heat performances, the SAR values recorded were in the range between 0.7 and 2.9 W/g.[23] Here, we have made an attempt to prepare 2D clusters using our high-performing IONCs[35] with sizes in the mesoscale range. Moreover, aiming to study the 2D structural transformation upon enzyme action, we have chosen an esterase-cleavable polymer that exploits the action of the lytic enzyme which is abundant in the tumor microenvironment.[36] For this purpose, we explored the aliphatic polyesters, polyhydroxyalkanoates (PHAs). PHAs are a group of highly biocompatible and bioresorbable polymers produced by a range of bacterial strains.[37,38] PHAs are susceptible to hydrolytic depolymerization including biocatalytic cleavage with enzymes such as esterases and lipases.[39,40] The enzymatic and hydrolytic cleavage of the ester bonds leads to PHA resorption in the human body. Hence, PHAs have been found to be particularly suitable for tissue engineering[41−43] and drug delivery[44−48] applications. There are two types of PHAs, short-chain length PHAs (scl-PHAs),[49] with C$_4$−C$_5$ carbon chain length monomers, and medium-chain length PHAs (mcl-PHAs),[50] with C$_6$−C$_{16}$ carbon chain length monomers. Here, we used a soft mcl-PHA copolymer in an oligomeric form (oligo-PHA; 10 kDa) because of its amphiphilic and resorbable properties[47,48,51] and good solubility in both hydrophobic and hydrophilic solvents. A wide range of suitable solvents for oligo-PHA enables utilization of this material in solution phase self-assembly methods.[52] Indeed, in this study, oligo-PHA enabled assembly of highly interactive IONCs into colloidal 2D structures (2D-MNBs). The properties of these 2D-MNBs were systematically compared to those of the same NCs in the form of both isolated NCs and 3D centrosymmetrical assemblies. The most remarkable features of the 2D-MNBs assembled with the assistance of natural polyester is the ability to disassemble into smaller assemblies of chains of NCs due to enzymatic cleavage of the polymer under biological conditions, and in turn, these chains doubled the heat efficiency (two-fold increase of the SAR value) at a well-defined incubation time point.

■ MATERIALS AND METHODS

Materials. Oligo-PHA, tetrahydrofuran (THF; 99%), nitrodopamine-poly(ethylene glycol) (PEG) carboxylic-terminated ligand (DOPA-PEG), triethylamine (TEA), toluene (99%), poly(maleic anhydride-*alt*-1-octadecene), PC18, M_n 30 000−50 000 (Aldrich), Milli-Q water (18.2 MΩ, filtered with filter pore size 0.22 μM) from Millipore, chloroform (CHCl$_3$, Sigma-Aldrich, 99%), iron(III) acetylacetonate (Acros Organics, 99%), decanoic acid (Acros Organics, 99%), dibenzyl ether (Acros Organic, 99%), squalene (Alfa Aesar, 98%), and liver porcine esterase(Sigma-Aldrich), fetal bovine serum (FBS). *Pseudomonas mendocina* CH50 used for the

production of PHA was obtained from the National Collection of the Industrial and Marine Bacteria (NCIMB 10541). For the production, characterization and hydrolysis of PHA ammonium sulphate, potassium dihydrogen phosphate, glucose, magnesium sulphate heptahydrate, methyl benzoate, and anhydrous sodium sulfate were purchased from Sigma-Aldrich (Dorset, UK), while disodium hydrogen phosphate, chloroform, methanol, and THF were purchased from VWR (Poole, UK). All chemicals were used as supplied without any further purification.

Synthesis of IONCs. IONCs with an edge length of 16 ± 2 nm were prepared according to previously reported protocol.[19,35] Briefly, 1 mmol (0.353 g) of iron(III) acetyl acetonate, 4 mmol (0.69 g) of decanoic acid, 7 mL squalene, and 18 mL of dibenzyl ether were dissolved in a 100 mL three-neck flask. After degassing for 120 min at 65 °C, the mixture was heated up to 200 °C at a rate of 3 °C/min, and this was maintained for 2.5 h. Later, the reaction temperature was raised to 310 °C (at a rate of 7° C/min), and the reaction continued for 1 more hour. Next, the solution was cooled down to room temperature, and 60 mL of acetone was added and centrifuged at a rate of 4500 rpm. After two washes, the dark pellet was redispersed in 15 mL of chloroform.

Production of mcl-PHAs by *P. mendocina* CH50. Mcl-PHAs were produced by *P. mendocina* CH50 (NCIMB 10541) using coconut oil as the sole carbon source, as described in Basnett et al., 2019.[53] The production was carried out in a 20 L bioreactor. The mcl-PHA copolymer was recovered from the freeze-dried biomass by a two-stage Soxhlet extraction process using methanol and chloroform as solvents. The polymer was precipitated in ice-cold methanol. The mcl-PHA produced was identified by gas chromatography−mass spectrometry and ^{1}H, ^{13}C NMR as the terpolymer of 3-hydroxyoctanoate, 3-hydroxydecanoate, 3-hydroxydodecanoate, and (poly(3-hydroxyactanoate-*co*-3-hydroxydecanoate-*co*-3-hydroxydodecanoate)) (Figures S1 and S2, Supporting Information). We will use mcl-PHA as the general abbreviation for this copolymer. The mole fractions for each monomer were found to be 0.30, 0.48, and 0.22 for 3-hydroxyoctanoate, 3-hydroxydecanoate, and 3-hydroxydodecanoate, respectively.

Hydrolytic Depolymerization of mcl-PHA. Hydrolytic depolymerization of the mcl-PHA copolymer was used for the preparation of the oligomeric derivative, oligo-PHA. mcl-PHA pellets (3 g) were added to a mixture of glacial acetic acid (166 mL) and deionized water (34 mL). Hydrolysis was carried out at 100−105 °C under reflux for 20 h. To quench the reaction, 200 mL of chilled deionized water was added to the reaction mixture. This produced an unstable emulsion of the product in aqueous media. The product was extracted using 300 mL of chloroform. Removal of water from the product solution in chloroform was conducted by adding crystals of anhydrous sodium sulfate. A clear solution of oligo-PHA in chloroform was concentrated by rotary evaporation. The residual chloroform was removed by evaporation at room temperature. The waxy oligo-PHA was dissolved in a small amount of THF. The oligo-PHA was reprecipitated by pouring into cold methanol kept in a crystallizing dish. After product settlement in the bottom of the dish and its walls, the solvent mixture with admixtures was decanted, and the oligo-PHA was dried in a vacuum oven at 40 °C.

Preparation of 2D-MNBs. Two-dimensional magnetic IONC assemblies (2D-MNBs) were prepared using a solution phase self-assembly method, following a protocol that was established by the Pellegrino group with few modifications.[52] Briefly, 30 μL of IONCs (edge length 16 ± 2 nm, 2.08 g_{Fe}/L in CHCl$_3$) was introduced into a 8 mL glass vial. Subsequently, 30 μL of oligo-PHA from a stock solution (2 mM in CHCl$_3$, 10 kDa) was added. After evaporating the initial solvents using N$_2$ flux, the materials were redispersed in 200 μL of THF, taken from a freshly opened bottle. After sonication for 30 s, the vial was fixed on an orbital shaker (rotating at 420 rpm), and 1.5 mL of Milli-Q water was dropped into it (0.5 mL/min). The magnetic nanostructures were then collected by placing the vial for 5 min on a permanent magnet (0.3 T). The magnetic material in the vial was recovered, and the supernatant was discarded. Finally, the obtained 2D-MNBs were promptly dispersed in 500 μL of distilled water and

filtered through a 5 μm hydrophilic filter. In order to obtain enough 2D beads for the hyperthermia measurements, this was repeated 40 times, and the magnetic materials merged together to reach an aqueous dispersion at a dose of 2.2 g/L based on iron.

Water Transfer of Individual IONCs for Comparison (Single NCs). The initial CHCl$_3$ dispersed IONCs were transferred into water using a standard protocol: the initial oleate surfactant on the particles was replaced with a nitrodopamine-PEG carboxylic-terminated ligand (DOPA-PEG), which had been prepared following a previously reported protocol.[54,55] For the water transfer procedure, 1.93 mL of DOPA-PEG (1500 MW, 0.05 M, i.e., 145 mg in 1.93 mL of CHCl$_3$, 150 ligand molecules/nm^2) and 1.93 mL of IONCs (2.08 g of Fe/L, 0.22 μM) that diluted to 1 g of Fe/L were mixed together in a 40 mL glass vial. Next, 947 μL of TEA was added dropwise. The mixture was then vigorously shaken overnight at room temperature. Afterward, the reaction mixture was transferred into a separation funnel, and 100 mL of toluene and 300 mL of Milli-Q water were added. After shaking and stabilizing the solution for 1 h, the lower aqueous phases, which contain the transferred particles, were collected and carefully purged thoroughly with nitrogen gas. The sample volume was reduced to 20 mL in a centrifuge, using 100 kDa centrifugal filters (Amicon filtering tube). Finally, it was dialyzed for 3 days against Milli-Q water (in the cellulose membrane with a MW cutoff of 50 kDa). The sample was then concentrated to adjust to the 3 g$_{Fe}$/L iron amount.

Synthesis of Standard 3D-MNBs. The standard 3D beads were produced by following our previously reported protocol, with minor modifications.[19] First, 18 μL of the IONCs solution (2.08 g$_{Fe}$/L in CHCl$_3$) and 33 μL of poly(maleic anhydride-*alt*-1-octadecene) (PC18) (50 mM in CHCl$_3$, i.e., referred to monomer units) were introduced to a 8 mL glass vial. Similar to the procedure that was used for 2D-MNBs, the solvent was evaporated from the mixture. Subsequently, the particles and polymer were redissolved in 200 μL of THF under sonication for 2 min. The vial was then fixed on an orbital shaker and was mixed at 1250 rpm, while 1.6 mL of Milli-Q water was dropped into it (4 mL/min). The final beads were transferred into water by collecting them with a permanent magnet (0.3 T) for 10 min. After discarding the supernatant, a brownish pellet of beads was dispersed in 500 μL of Milli-Q water. To scale up the amount of beads for MH, this protocol was repeated 60 times, and the beads were merged together to reach a final concentration of 3 g$_{Fe}$/L.

Quantification of Iron. To compare the different samples, their iron content was quantified by elemental analysis using an inductive-coupled plasma atomic emission spectrometer (ICP-AES, iCAP 6500,/ Thermo). Prior to the measurements, the samples were subjected to overnight digestion in aqua regia before being diluted with water for the final analysis.

Dynamic Light Scattering. The hydrodynamic sizes of the nanostructures were determined using Zetasizer Nano ZS90 (Malvern, UK), which operated at 633 nm and was equipped with a He−Ne laser (4.0 mW) and a photodiode detector. The results were reported as an average of three repeated measurements.

Transmission Electron Microscopy Imaging. The structure and morphology of the nanostructures were investigated under transmission electron microscopy (TEM; JEOL JEM-1011), which operated at an accelerating voltage of 100 kV. Diluted aqueous solutions of samples were deposited by drop-casting, and they were allowed to dry under room temperature for 12 h. In addition, for the 2D-MNBs, a separate grid was prepared and stained with uranyl acetate so that it would contrast better with the polymeric shell.

Cryo-TEM and Cryo-Electron Tomography of 2D-MNBs. Frozen hydrated samples were prepared by applying a 3 μL aliquot of 2D-MNBs to a previously glow discharged QUANTIFOIL holey carbon grid (Cu 200 mesh 2/1, Nanovision, Italy). The grids were vitrified into liquid ethane using a FEI Vitrobot Mark IV cryo-plunger (Thermo Fisher Scientific, USA). Images of the samples were taken at cryogenic temperature (−170 °C) using a Tecnai F20 microscope-(Thermo Fisher Scientific, USA), equipped with a Field Emission gun operating at an acceleration voltage of 200 kV, with a US1000 Gatan CCD camera and an FEI automatic cryo-box. For the cryo-electron tomography (CET), the tilt series were collected by tilting the

vitrified sample over $\pm 66°$ with the following tilt sequence: starting from $0°$ to ± 48 with a tilt step of $3°$; then from ± 48 to $\pm 66°$ with a tilt step of $2°$. The cryo-EM imaging was carried out at a final object pixel of 3.6 Å, with a total dose of ~ 90 e⁻/Å² in order to limit specimen damage. Computation of the tomogram was carried out with the IMOD software package using a WBP-based algorithm.[56] Segmentation and 3D visualization were carried out using the Amira package (Thermo Fisher Scientific, USA)."

Magnetic Accumulation Experiment. In three disposable cuvettes, the required amounts of single NCs, the 2D-MNBs, and the 3D-MNBs were dispersed in 500 μL of deionized water in order to produce suspensions containing the same amount of the magnetic material (40 μg of iron). Each sample was simultaneously exposed to a permanent magnet (0.3 T). The three vials were photographed with a digital camera after 80 s for 2D-MNBs, after 120 s for 3D-MNBs, and after 24 h of magnetic exposure for the single NC.

Magnetophoretic Mobilities of 2D-MNBs. To derive the magnetophoretic velocity of the 2D-MNB and 3D-MNB samples, a magnetic attractor was used.[24] A nickel wire with a diameter of 50 μm was placed in a chamber, and it was submitted to a magnetic field of 0.2 T (which saturates the magnetization of the nano-objects). The magnetic field gradient that developed in the proximity of the wire was carefully calibrated using 1 μm beads (Dynabeads, MyOne). The individual nano-objects that were attracted to the wire were tracked when they passed through an observation window that was situated at a distance of 100 μm away from the wire extremity. At this distance, the magnetic field gradient (grad B) was 200 T/m. The migrating nanobeads' viscous drag force can be calculated using the formula $3\pi\eta d_h v$ (in which η is the fluid viscosity 10^{-3} Pa·s, d_h is the hydrodynamic diameter of the nanobead as measured by dynamic light scattering (DLS), and v is its measured velocity), and this should be equal to the magnetic force $m$grad B (in which m is the nanobead magnetic moment at saturation). This magnetic moment m is therefore directly inferred from the value of the velocity. Such measurements were averaged over 100 nano-objects and were repeated three times.

$$m = \frac{3\pi\eta d_h v}{\text{grad } B} \quad (1)$$

Calorimetric SAR measurements on single NCs and 2D and 3D-MNBs. The heating efficiency of water-dispersible single NCs and 2D and 3D-MNBs was evaluated by calorimetric and magnetic measurements. Calorimetry measurements were performed at different fields (range from 12 to 30 kA m⁻¹) and frequencies (110−300 kHz) using DM 100 series (nanoScale Biomagnetics Corp), a commercially available instrument. For the measurements, 300 μL of an aqueous suspension of the samples (at a concentration of Fe in the range of 2.2−3 g/L) was first sonicated for 1 min; then they were introduced into the sample holder. Before starting the measurement, the sample temperature was recorded for 5 min until it attained a stable value. Upon the application of the AMF, the temperature versus time curves were recorded using an optic fiber thermosensor (LumaSense). The heating performance of nanostructures were quantified in terms of SAR values by the initial slope (within the first few seconds) of the temperature versus time curve using the equation below

$$\text{SAR (W/g}_{Fe}) = \frac{C}{m_{Fe}} \frac{m_d dT}{dt} \quad (2)$$

where C is the specific heat capacity of water (C_{water} = 4.18 J g⁻¹ K⁻¹), and m_{Fe} is defined as the iron mass per g of the dispersion, and m_d is the mass of the dispersion.

SAR of 2D-MNBs after Enzymatic Cleavage. We investigated the trend of SAR variations in 2D-MNBs after enzymatic cleavage as a function of the incubation time upon exposure to liver porcine esterase at 37 °C. For this experiment, a frequency (f) of 300 kHz and a magnetic field amplitude (H) of 16 kA m⁻¹ were the AMF parameters within the clinically acceptable limit (the $H \times f$ product was below 5×10^9 A m⁻¹ s⁻¹).[57,58] For the enzyme experiment, 300

μL of 2D-MNBs dispersed in water (2.2 g_{Fe}/L) were incubated at a physiological temperature of 37 °C with a 70 μL aliquot of the esterase enzyme that had been extracted from porcine liver (2 mg/mL and commercially available). The SAR values of the 2D-MNBs were investigated at several points of incubation from 0.25 to 48 h. The influence of the enzyme on the overall bead morphology and stability was traced using DLS and TEM.

ac Magnetometry Measurements. Magnetometry measurements were carried out at a fixed iron concentration of 1 g_{Fe} L⁻¹, using frequencies of 30, 100, and 200 kHz, and a magnetic field amplitude of 24 kA m⁻¹ at room temperatures. ac hysteresis loops were traced with a home-made inductive magnetometer based on the one described by Connord et al.[59] The values of ac magnetization were normalized to the mass of the magnetic element (i.e., iron). ac hysteresis loop measurements consist three repetitions to obtain an averaged and standard deviation of the magnetic area values. Afterward, SAR values were calculated according to SAR = $A \cdot f$,[60] where A is the magnetic area, and f is ac magnetic field frequency. In addition, the aggregation effects on the ac hysteresis loops were analyzed under the same conditions, with FBS volume fractions of 13, 55, and 27% (v/v) for single NCs and 2D and 3D MNBs, respectively.

Cell Culture. A431 epidermoid carcinoma cells (ATCC CRL-1555) were cultured in Dulbecco's modified Eagle's medium (high glucose) supplemented with 10% FBS (heat inactivated FBS), 2% penicillin−streptomycin (10 000 U/mL), and 1% L-glutamine (200 mM) at 37 °C, 5% CO_2, and 95% relative humidity. All cell culture reagents were purchased from Gibco.

Evaluation of 2D-MNB Heat Loss in Tumor Cells. To establish heat loss, 5 million A431 cells in 25 μL of complete media, simulating a small tumor mass, were supplemented with 2D-MNBs (50 μL 2 mg_{Fe}/mL) and an esterase enzyme solution (25 μL of 2 mg/mL). This sample was divided into two parts. In one part (50 μL, sample named A431+2D-MNBs_no incubation), the ac hysteresis loop (at 300 kHz and 16 kA m⁻¹) or the MH treatment was immediately performed (at a frequency of 300 kHz and a magnetic field intensity of 16 kA m⁻¹ for three cycles of 30 min each with a 5 min break in between each cycle). The second part (50 μL) was incubated for 3 h at 37 °C to enable the enzymatic digestion of the polymer (the "A431+2D-MNBs_3h-incubation" sample). Soon after the incubation, the ac hysterics loops were measured at 300 kHz and 16 kA m⁻¹ on an ac magnetometer.

In Vitro MH Treatment and Cytotoxicity Assay. A431 cells (5×10^6 cells in 25 μL of complete media) were supplemented with 50 μL of 2D-MNBs (2 g_{Fe}/L) and with 25 μL of esterase enzyme (2 g/L) as a cleaving agent for 2D-MNBs. This sample was divided into two parts: one part was immediately exposed to alternative magnetic fields of 300 kHz and 16 kA m⁻¹ (3 cycles of 30 min each) using an MH setup (DM100 series, nanoScale Biomagnetics). The second part was first incubated for 3 h at 37 °C, and then it was exposed to MH treatment. After the MH treatment, the cells were reseeded on 12-multiwell plates (2.5×10^6 cells/well), and the cell viability was assessed by trypan blue assay 24 and 48 h post MH treatment. The first control group consisted (i) cells (5×10^6 cells/well) treated with porcine esterase (no 2D-MNBs, no MH) in the cell culture medium maintained at room temperature for 100 min (equivalent time needed for MH treatment) (t_0) before being reseeded for the evaluation of cell viability at 24 and 48 h; (ii) cells (2.5×10^6 cells) treated only with porcine esterase (no 2D-MNBs, no MH) incubated at 37 °C for 3 h (t_{3h}). After the time of incubation, they were maintained at room temperature for 100 min (t_{3h}) before reseeding them. The second group consisted of cells treated with 2D-MNBs, porcine esterase (no MH), and maintained at room temperature for 100 min (t_0, 2.5×10^6 cells) before reseeding. Also, in this group, cells (t_{3h}, 2.5×10^6 cells) were treated with 2D-MNBs and porcine esterase (with no exposure to MH) and then incubated for 3 h at 37° (t_{3h}). After this incubation time, the cells were maintained at room temperature for 100 min before being reseeded for cell viability assay. The third group consisted of cells treated with 2D-MNBs and porcine esterase which were then exposed to MH. For these groups, we have considered a first group that consisted of cells mixed with 2D-MNBs and porcine
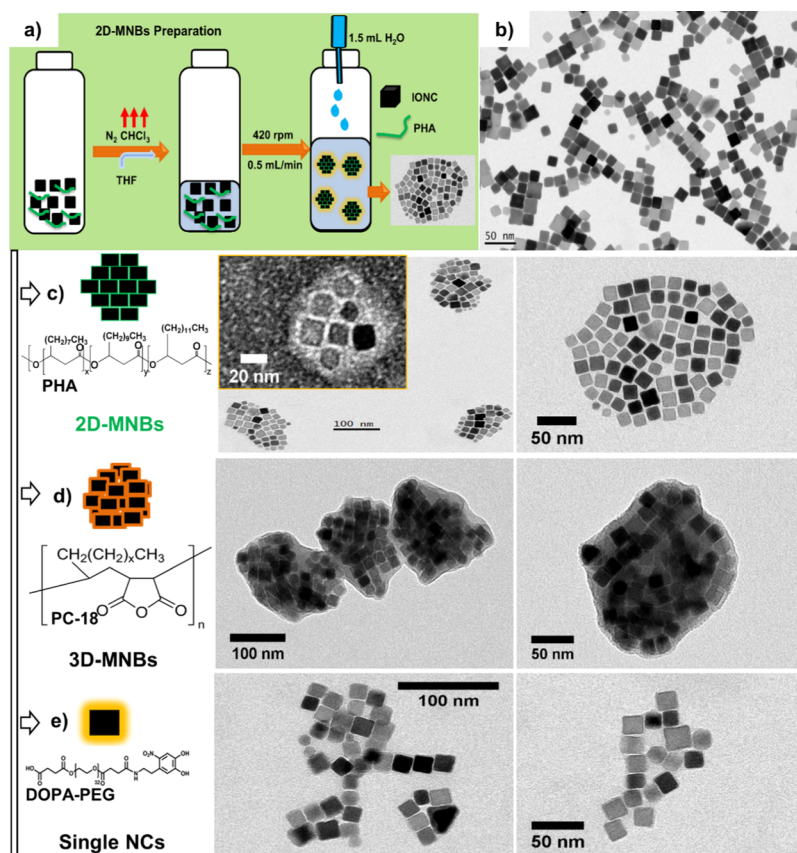
Figure 1. Preparation and imaging of water soluble 2D-MNBs: (a) schematic representation of the protocol to prepare 2D-MNBs. (b) TEM image of the initial IONCs with an edge length of 16 ± 2 nm, dispersed in chloroform. (c) TEM images of 2D-MNBs obtained from a water solution. Insets: images of higher magnification. The left inset was obtained after staining the grid with uranyl acetate in order to stain the polymer (bright shadow around NCs). (d) TEM images of 3D-MNBs. (e) TEM images of water-transferred single cubes (single NCs), which were obtained by means of the ligand exchange method using the same batch of NCs. The grouping of single NCs on the grid is purely a drying effect, as the single-coated NCs (single NCs) have a small hydrodynamic size (30 ± 8 nm, Table 1 & Figure S3).

---

esterase and directly exposed to MH (2.5×10^6 cells), while for the other group (t_{3h}) the cells were mixed with 2D-MNBs and porcine esterase, incubated at 37 °C for 3 h and only after incubation, they were exposed to MH treatment.

RESULTS AND DISCUSSION

With the clear goal of identifying the most suitable materials for MH, the development of assembly protocols of MNPs into structured architectures has recently gained specific attention in the scientific community.[61−63] The focus of this research is on the understanding of how heat efficiencies and thus SAR values change when MNPs are arranged in well-defined structured geometries.

As presented in Figure 1a, we have established an assembling protocol to turn IONCs into two-dimensional structures (2D-MNBs) using a biodegradable oligo-PHA with a molecular weight of 10 kDa. Initially, a chloroform dispersion of IONCs (with a cubic length of 16 ± 2 nm, Figure 1b) was mixed with the oligo-PHA solution in chloroform (2 mM). After the chloroform solvent had completely evaporated, THF was added. The initial polymer/NP ratio was fixed to a value of 7, considering a ratio of polymer chain per nm² of the NC surface. Then, a 30 s sonication step helped to improve the dispersion of the materials. Later, under mild shaking on an orbital shaker (420 rpm), 1.5 mL of Milli-Q water (0.5 mL/min) was added as an antisolvent. The change in the polarity, which was promoted by adding water to the THF solution

containing the PHA polymer and the IONCs, caused a conformational rearrangement of oligo-PHA and a controlled precipitation of the NCs; the alkyl chains of the polymer intercalate with the hydrophobic capping ligands of the IONCs, producing an orderly 2D pattern of NCs (Figure 1c for a TEM characterization of the clusters). Control experiments confirmed the importance of the oligo-PHA as a directing agent to induce the 2D-MNB formation. Indeed, by repeating the 2D-MNB protocol in the absence of any PHA polymers (i.e., only in the presence of IONCs), large 3D aggregates of IONCs precipitate out of the solution (Figure S3a). By repeating the protocol in the presence of only a PHA polymer (i.e., with no IONCs in the solution), an opaque polymer solution is still obtained, and it contains some flake-like polymer structures (Figure S3b). To control an ordered IONC assembly in 2D-MNB, the assembly rate at which the water is added to the THF polymer−IONCs mixture is extremely important. For instance, when the 2D-MNB protocol was performed at a higher water addition rate (4 mL/min and 1250 rpm shaking speed rather than 0.5 mL/min as is standardly used for 2D-MNBs), it produced floating flakes of insoluble samples that contained very large and irregular IONC structures, as was seen under TEM (Figure S3c, Supporting Information). However, the PHA polymer is also very important with regard to driving the 2D assembly. Indeed, when the standard 2D-MNB protocol was applied, but PC18-was used rather than PHA as the polymer, very large water-

soluble 3D clusters were obtained rather than controlled 2D-MNB assemblies (Figure S3d, Supporting Information). Overall, these data highlight the key role of oligo-PHA in driving the 2D assembly of IONCs, and they demonstrate that it is extremely important to use a low water addition rate (0.5 mL/min) to form 2D-assemblies. Here, similar to Zhang et al. work, we hypothesize that the linearity[64] and amphiphilic properties of the oligo-PHA, together with our working parameters promote bidimensional self-assembling IONCs.[65] Finally, to remove any excess of the oligo-PHA, the beads were collected twice to a permanent magnet (0.3 T). The black pellets were attracted to the magnet, and the supernatant was discarded with a final pellet redispersion in Milli-Q water. Thanks to the rapid magnetic response of the 2D-MNBs (80 s) the cleaning steps were easy and quick. The reproducibility of the 2D-MNBs was affected by the quality of THF. Indeed, when the 2D-MNBs were synthesized using fresh THF, the 2D-MNB structures were the major fraction while aggregates formed when a THF bottle that was aged and kept outside the glove box was used (the bottle was opened 45 days before, and minor traces of impurities were noted in NMR, see Figure S5, Supporting Information). This was not the case when we made 3D-MNBs using the same batches of NCs and an amphiphilic polymer, namely, poly(maleic anhydride-*alt*-1-octadecene) (PC18, 30−50 kDa) following our previously developed protocol (Figure 1d).[19,52] We may assume that the wetting behavior of IONCs with oligo-PHA or IONCs with PC18 is different and the IONCs−oligo-PHA interactions were more affected by the humidity than in the case of PC18 employed for making 3D-MNBs. The choice of cubic shape MNPs has a significant impact on the final ordering of the structure. To give a simple example, in addition to using an IONC sample with a more regular shape and a cube edge of 16.0 ± 1.8 nm, we also carried out a control experiment using IONCs that have an irregular shape (16.0 ± 2.7 nm). The resulting assemblies still had a bidimensional arrangement, but they showed an imperfect ordering, indicating that the face-to-face cube interaction is important to control the 2D-MNB arrangements (Figure S6, Supporting Information). To scale up the production of these 2D-MNBs, the described protocol was repeated 40 times, and the 2D-MNBs were collected by the magnet and combined together in 10 mL of water. The final sample was filtered through a 5 μm hydrophilic filter. After filtration, the 2D-MNB concentration was adjusted to 3 g_{Fe}/L. It is worth mentioning that prior to using the 10 kDa polymer, preliminary attempts were made using a native mcl-PHA of a larger molecular weight (ca. 333 kDa). With such a high molecular-weight polymer, 3D clusters rather than 2D clusters were obtained (Figure S7, Supporting Information), and they were poorly dispersible in water. Polymers with a larger molecular weight have lower solubility in THF than the short oligo-PHA polymer and this might have affected the interactions of the polymer with the IONCs and the resulting geometry of the clusters. Moreover, they tend to collapse randomly and rapidly in presence of NCs, consequently forming 3D clusters.

To compare the MH efficiency of the 2D-MNBs to that of single NCs, we transferred the same batch of IONCs in water through a ligand exchange protocol using DOPA-PEG as the stabilizer molecule (Figure 1e).[35] In comparison to 3D-MNBs, 2D beads have a thinner polymer shell as shown by TEM using uranyl acetate staining (see Figure 1c, left inset). In order to confirm the presence of 2D-MNBs in suspension and minimize

the artifacts that affect conventional TEM, we characterized the 2D-MNBs in the suspension by cryo-TEM. The analysis performed on a vitrified sample clearly showed the presence of bidimensionally ordered NC assemblies in their fully hydrated state (see Figure 2a,b). To further investigate the geometry of
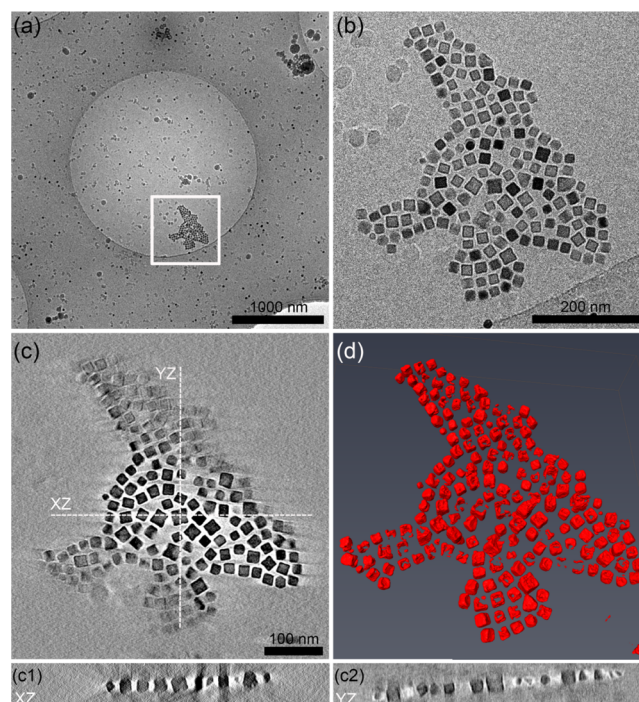

Figure 2. Cryo-TEM and CET. (a) Low magnification projection cryo-TEM image of a vitrified 2D assembly. (b) Higher magnification of the region outlined in (a). (c) *XY* CET tomographic averaged slice (*n* = 10) of the 2D assembly shown in (a,b). (c1,c2) are *XZ* and *YZ* slices sections, respectively (*n* = 10) of the tomogram in (c). (d) Reconstructed 3D model from the tomogram in (c). These data confirm the presence of 2D-MNBs in the solution, forming a clear bidimensional monolayer assembly of IONCs.

these assemblies, we performed CET. CET analysis explicitly revealed that the 2D-MNBs in solution are organized in a monolayer of IONCs with a well-ordered 2D assembly (see Figure 2c,d and the Movie 1.mp4).

The assemblies' mean values of 393 ± 117 and 171 ± 64 nm (DLS size weighted by the number percent) correspond to the 2D-MNBs and 3D-MNBs, respectively, larger than the TEM size core as they include the hydrated polymer. The narrow polydispersity index (PDI) values of hydrodynamic size implied good colloidal stability and no clustering in water dispersion (Table 1). TEM results suggest that 2D-MNBs contain IONCs with constant spatial distance between NCs

Table 1. Summary of Average Hydrodynamic Sizes of All Three Structures (i.e., Single NCs, 2D-MNBs, and 3D-MNBs) in Water, as Measured by DLS

sample	number d.nm	intensity d.nm	volume d.nm	PDI
single NCs	30 ± 8	57 ± 24	39 ± 14	0.344
2D-MNBs	393 ± 117	452 ± 129	495 ± 148	0.074
3D-MNBs	171 ± 64	227 ± 76	250 ± 91	0.101
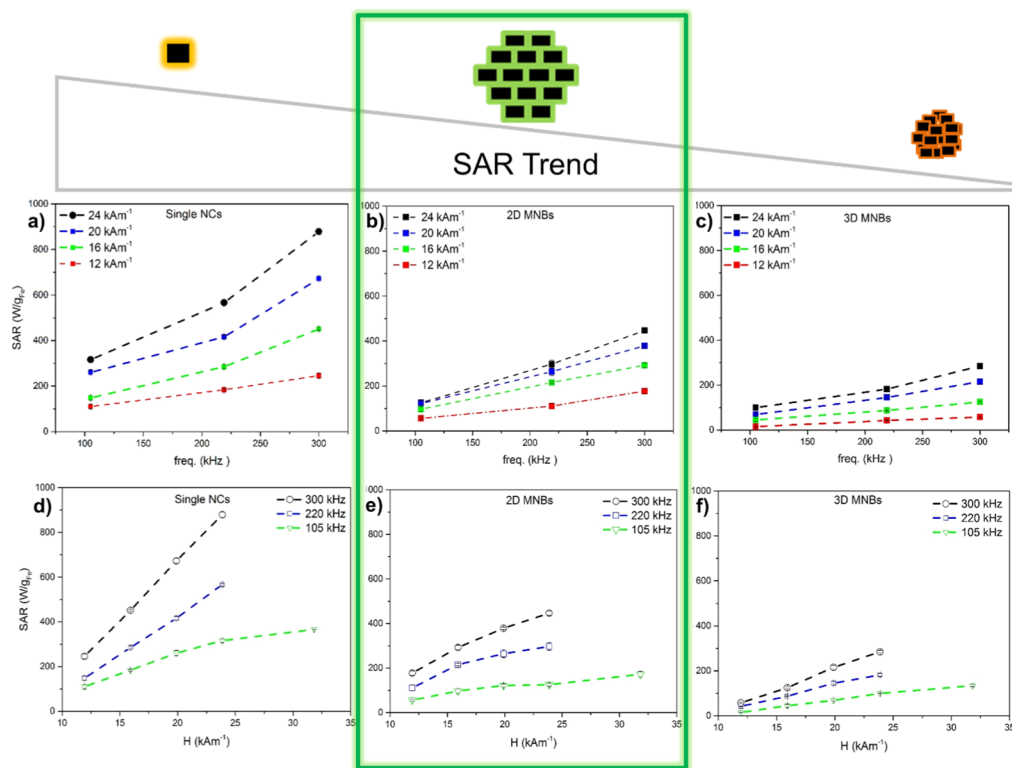
Figure 3. SAR values of single IONCs, 2D-MNBs, and 3D-MNBs in water: (a−c) Field frequency dependence of SAR values (W/g$_{Fe}$) for single NCs, 2D-MNBs, and 3D-MNBs for different field amplitudes in the range from 12 to 24 kA m^{-1}. (d−e) Field intensity dependence of SAR values for single NCs, 2D-MNBs, and 3D-MNBs at different field frequencies (105, 220, and 300 kHz). The green frame highlights the novel 2D structures developed in this work.

inside the structure, but this is not the case for 3D-MNBs, in which the IONCs are densely and randomly packed.

Figure 3 presents the comparison of SAR values of single NCs, the 2D and 3D-MNBs dispersed in water obtained by calorimetric measurements at different field conditions and at similar iron concentration (3 g$_{Fe}$/L) for the three types of MNP assemblies. At a first glance, SAR values are different among the assemblies, showing significant reductions from single NCs to 2D-MNBs, and more significant for 3D. This probes the correlation between SAR values and MNP clustering arrangement. Indeed, the 2D-MNBs show SAR values lower than single IONCs but almost double those of 3D-MNBs. This tendency is preserved for all applied field conditions (see Figure 3).

For example, at 300 kHz and 24 kA m^{-1}, 2D-MNBs show a SAR value of 443 ± 9 W/g, which is more than 30% higher than the one of 3D-MNBs (284 ± 5 W/g), 50% lower than for single IONCs. Such clustering effect on the SAR value can be understood in terms of the different magnetic dipolar interactions related to distinct IONC spatial distribution within the 2D and 3D aggregates.[21,61] Thus, in a 2D-MNB, the spatial order of IONCs into the cluster and the constant interparticle distance minimize magnetic dipolar interactions, resulting in SAR values that are closer to that of single IONCs (see the TEM image in Figure 1) than in the case of 3D-MNBs, where IONCs are randomly distributed into all spatial directions in the cluster. The latter causes significant demagnetization effects, which would directly reduce the SAR performance.[19,20,66]

To complement the calorimetric SAR characterization, ac magnetometry was employed to probe the same samples at

similar iron concentration (1 g$_{Fe}$/L) and field conditions (from 30 to 200 kHz). Figure 4 shows ac hysteresis loops of the three distinct assemblies dispersed in deionized water and in FBS diluted solutions. In water dispersions, the ac hysteresis loops of single IONCs have larger magnetization and area values at maximum field than 2D-MNBs. The latter shows similar magnetization values but larger area values than 3D-MNBs at all employed field conditions. Considering SAR = A·f,[60] the observed magnetic losses are gradually reduced from single IONCs, 2D-MNBs, and 3D-MNBs, in agreement with the calorimetric SAR measurements (Table S1, Supporting Information).

The dilutions with FBS intentionally induced aggregates that would somewhat resemble the conditions in a cellular environment.[4,67] The occurrence of aggregation in FBS was confirmed by DLS measurements as z-average values, whose basic hydrodynamic sizes shifted toward higher ranges for all assemblies (see the hydrodynamic values in Figure 4). In spite of the different hydrodynamic values, images shown in the right and left panels of Figure 4 directly exhibit the colloidal stability of the assemblies before and after the addition of FBS. It is remarkable that, for 2D-MNBs, the hysteresis loop area/ shape remained almost unaltered when the hydrodynamic size was doubled from 422 to 816 nm (Figure 4d, green panels). On the contrary, the single-NC and the 3D-MNB structures precipitate when the hydrodynamic size is increased but only single NCs show significant variations of ac hysteresis loops (shape and area) and no change for the 3D-MNBs. This can be understood as a boasting of magnetic dipolar interactions when increasing the assembly aggregation, whereas for 2D-MNBs and 3D-MNBs, the random interparticle distance is frozen per
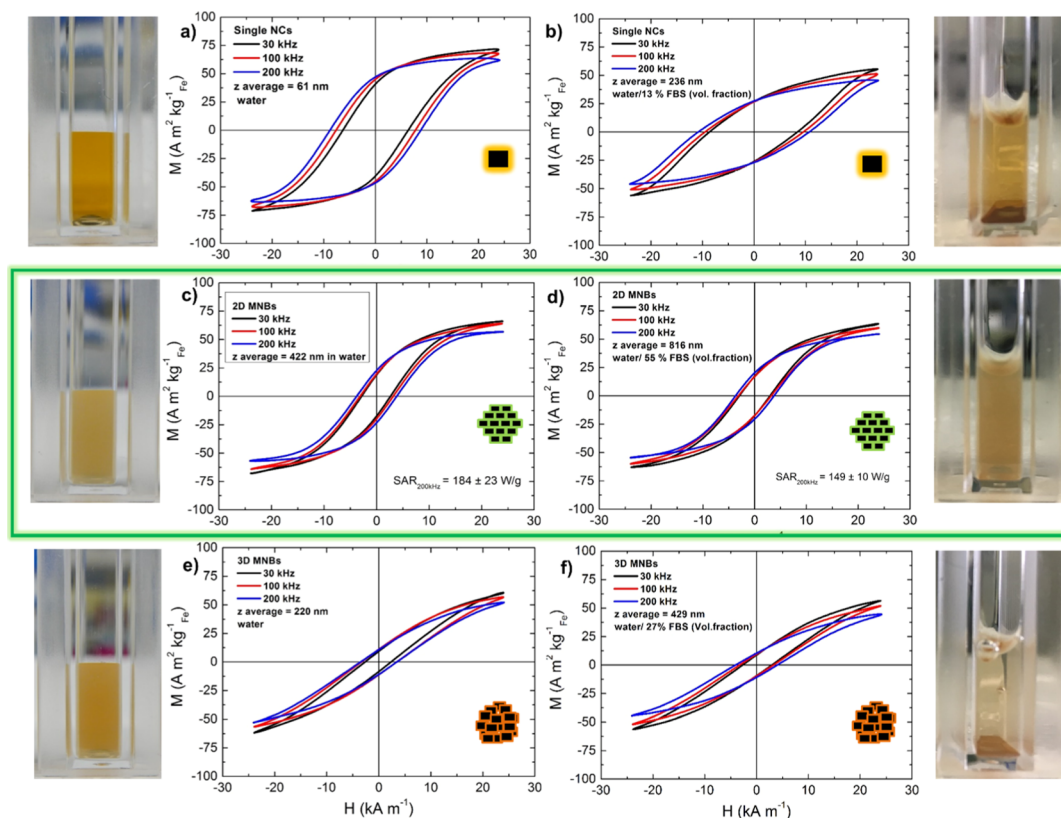
Figure 4. ac Hysteresis loops of single NCs, 2D-MNBs, and 3D-MNBss in water (left panels) and in FBS (right panels) at different frequencies. (a) ac hysteresis loops of single NCs dispersed in water. (b) ac hysteresis loops of single NCs dispersed in an aqueous 13% FBS solution. (c) ac hysteresis loops of 2D-MNBs dispersed in water and (d) in aqueous 55% FBS solution, (e) ac hysteresis loops of 3D-MNBs dispersed in water and (f) 3D-MNBs in aqueous 27% FBS solution. The images on the left and right panels correspond to the assemblies dispersed in water (left) and in the corresponding FBS (right) solutions.
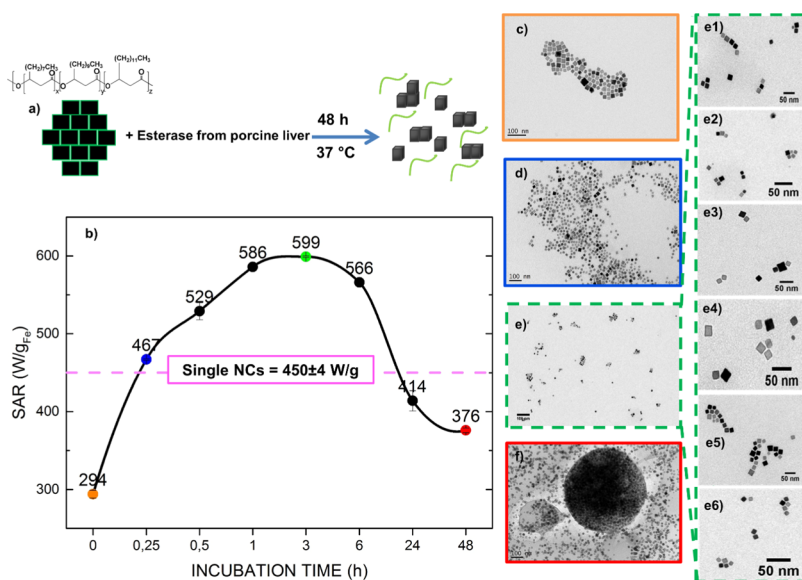
Figure 5. SAR values of 2D-MNBs exposed to esterase enzymes at different incubation times. (a) Graphical representation of the esterase-mediated cleavage of 2D-MNBs (300 μL, 2.2 g_{Fe}/L), incubated at 37 °C. (b) Plot defines the variation in the SAR as a function of incubation time with esterase, measured at 300 kHz, 16 kA m^{-1} (which is below the biologically acceptable limit $H_f = 5 \times 10^9$ A m^{-1} s^{-1}). The horizontal dashed line corresponds to the SAR value of single IONCs (450 ± 4 W/g). The TEM images on the right panel indicate the structural morphology of cleaved 2D-MNBs at different time points of incubation, including (c) 0 h (before the addition of enzyme, highlighted in orange), (d) 0.25 h (blue), (e) 3 h (green), and (f) 48 h (red). Additional images framed in green (e1−e6), correspond to the sample at 3 h. At this time point, small chains of NCs appeared, which may explain how the highest SAR recorded was achieved, owing to their unique structural arrangements.
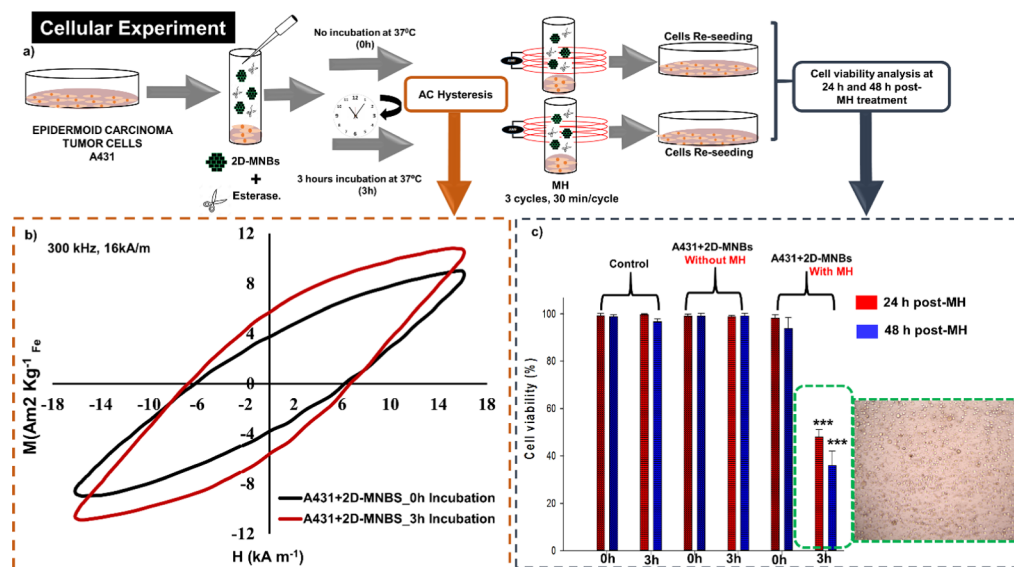
Figure 6. In vitro cellular experiments. (a) Graphical scheme summarizing the cellular experiment. In vitro hyperthermia studies on an A431 cell line incubated with 2D-MNBs and esterase. (b) Comparison of ac Hysteresis loops recorded for the cell samples before (A431+2D-MNBs_0h incubation) and after incubation (A431+2D-MNBs_3h incubation) at 37 °C. Even in the presence of tumor cells, the hysteresis loop is larger for the sample that had been incubated with enzymes (red curve) than for the sample that was not incubated at 37 °C (black curve). (b) Cell viability study evaluating the cytotoxic effects with or without exposure to MH for A431+2D-MNBs_0h-incubation and for A431+2D-MNBs_3h-incubation. The viability was assessed after re-culturing the A431 cells after 24 and 48 h. The MH was performed at 300 kHz and 16 kA m^{-1}. (c) Inset: representative optical image of A431 cells exposed to A431+2D-MNBs_3h-incubation and after MH treatment. Many detached round cells are present.

cluster in spite of their aggregation, and the ac hysteresis loops are strongly influenced by the aggregation of single NCs (i.e., larger hydrodynamic size and stronger dipolar interaction). The result observed for 2D-MNBs that the aggregation of individual clusters does not significantly influence the ac hysteresis in spite of the fact that their planar MNP spatial configuration is quite unexpected. The latter could explain that in the particular case of magnetic planar arrangement of individual MNPs, magnetic moments result in no significant interacting effects between 2D-MNBs.

For the 2D-MNBs, in addition to the limited variation by ac dynamic hysteresis of the loop area and as well as the magnetization at the maximum field, as measured by direct calorimetric measurements, it corresponded to a limited reduction of SAR at 200 kHz from the water-dispersed state (184 ± 23 W/g) to FBS (149 ± 10 W/g). This experimental evidence confirm the SAR aggregation-free behavior of the 2D-MNBs (refer to Figure 4c,d). This feature is very important because most of the nanoclusters show significant variations in their magnetic losses with drastic reduction of the magnetic heat performances when their aggregation increases, limiting their MH performance in a cellular environment.[4,68]

In order to show the spatial distribution effects on the SAR values of 2D-MNBs, we exploited the biodegradability properties of oligo-PHA polymers when exposed to lytic enzymes. Thus, we treated the 2D-MNBs with a porcine-derived esterase enzyme at 37 °C, monitoring the SAR at different times over 48 h of incubation (Figure 5a). Surprisingly, the SAR values for the 2D-MNBs that were recorded within the first 3 h of incubation dramatically increased and almost doubled in value (599 ± 1 W/g) with respect to the those of the initial 2D-MNBs (294 ± 5 W/g). After 3 h of exposure to esterase, the SAR of the 2D-MNBs increased even more than that of single NCs (450 ± 4 W/g). At longer incubation times, the SAR started to progressively

decrease until, at 24 h, it reached a value that was never less than the initial value of 294 W/g (Figure 5b).

We also investigated the structural differences in the 2D-MNBs at different incubation time points. Initially, after 15 min of enzyme treatment, the structures gradually began to lose their 2D shape, and IONC spatial distributions on the grids looked similar to those of single NCs (Figure 5d). Interestingly, even the SAR value (467 ± 1 W/g) at 15 min resembled that of single NCs (450 ± 4 W/g). Later, at 3 h of incubation, the TEM images showed the presence of chain-like configuration (Figure 5e,e1−e6), which was accompanied with an increase of the SAR value, which doubled (599 ± 1 W/g) that of the initial 2D-MNBs (294 ± 5 W/g). Such SAR increase can be understood as an effect of the disassembling of 2D-MNBs induced by the enzyme. As shown in Figure 5e, the short chains of IONCs are observed. As a result of the magnetic dipolar coupling, the short chains of IONCs behave as elongated entities with a single and large magnetic momentum, whose magnetic easy axis responds quickly to magnetic fields. Moreover, in such a short chain configuration, the shape anisotropy of the structure also improves. Consequently, the heating abilities are better than those of isolated IONCs (which have no dipolar interaction) and 3D-MNBs (which have a random dipolar interaction). These results are supported by other theoretical and experimental studies.[21,69−71] However, it is remarkable that the absolute SAR values that had previously been recorded were lower than the ones reported herein due to the poorer magnetic quality of the initial nanocrystals used for the chain assemblies (core−shell wustite/iron oxide particles or spherical iron oxide nanoparticles).

At incubation times of 24 and 48 h, TEM revealed the presence of NCs both as individual and NCs forming some aggregates (highlighted in red, Figure 5f). These observations support the progressive decrease in the SAR that was recorded
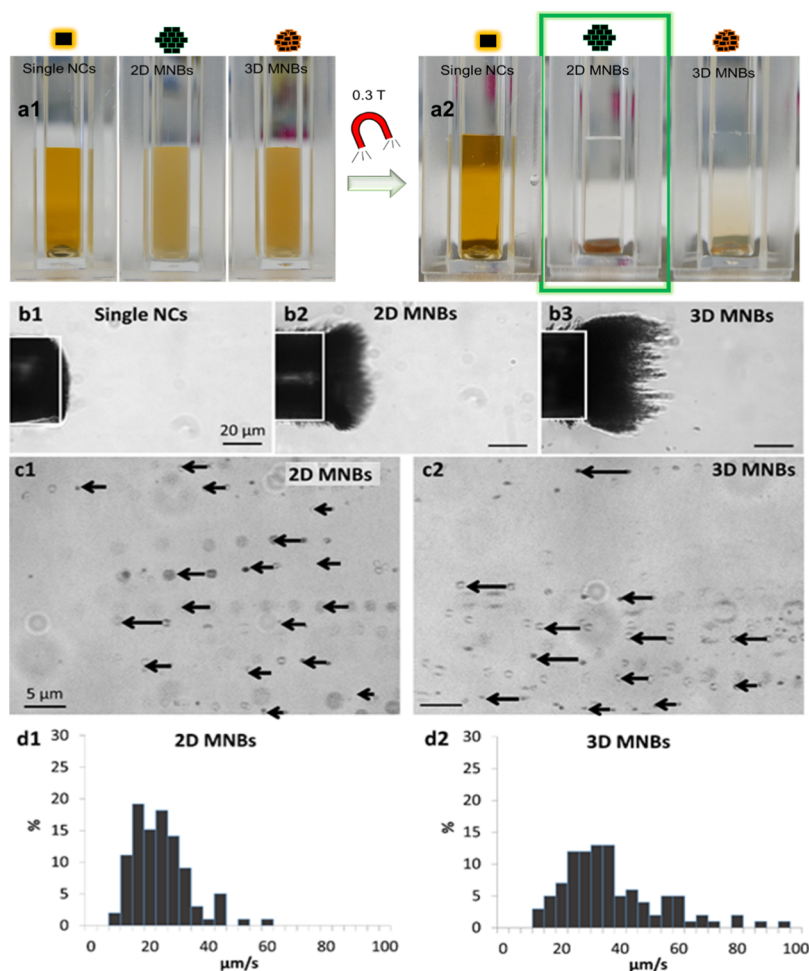
Figure 7. Magnetic accumulation and magnetophoretic mobility: (a1) Picture of single NCs, 2D-MNBs and 3D-MNBs dispersed in 500 μL of water (each with 40 μg of Fe) before and after exposure to a magnet (0.3 T) for 24 h, 82 s, and 120 s respectively. (b) Attraction by a magnetic nickel tip magnetized in a 0.2 T magnetic field of single NCs (b1, no tip covering), 2D-MNBs (b2) and 3D-MNBs (b3). (c) Magnetophoretic motions of the 2D-MNBs (c1) and 3D-MNBs (c2) toward the magnetic tip. Each image is the superimposition of successive images separated by 100 ms each. Arrows illustrate the displacement of single NBs in between two images, directly proportional to the magnetic velocity. (d) Histograms of the magnetophoretic mobility in terms of μm/s, for 2D-MNBs (d1) and 3D-MNBs (d2).

at the 24 and 48 h time points. It is worth highlighting that, as some structural modifications occurred, the dispersibility in water was progressively affected, especially after the first few hours (Figure S8, Supporting Information).

To estimate the magnetic heat loss on the cells and the heat damage effects induced by MH treatment in the case of both the 2D-MNBs and the disassembled chains upon enzymatic action, an in vitro cellular experiment on epidermoid carcinoma cells (A431) was conducted. To this end, 5 million A431 cells, simulating a small tumor mass, were supplemented with 2D-MNBs and an esterase enzyme solution, the latter of which was added to enable polymer digestion. This sample was divided into two parts. On one fraction (sample named A431+2D-MNBs_0h-incubation), the ac hysteresis loop was directly recorded (300 kHz and 16 kA m^{-1}). The second part was first incubated for 3 h at 37 °C to enable the enzymatic digestion of the polymer (referred as "A431+2D-MNBs_3h-incubation"). Immediately after the incubation time, the ac hysterics loops were recorded (Figure 6b). The ac measurements (Figure 6b) clearly indicate that the sample A431+2D-MNBs_3h-incubation, which was incubated for 3 h at 37 °C, has a larger hysteresis loop than the A431+2D-MNBs_0h-incubation sample that was not incubated at 37 °C. This was

also reflected in the SAR values, which were calculated by considering the area of the hysteresis loops for both the A431+2D-MNBs_3h-incubation sample and the A431+2D-MNBs_0h-incubation sample (Figure S9).

Moreover, these data are also supported by the cytotoxicity heat damage, which was recorded after having performed the MH treatment. In a parallel experiment, the A431+2D-MNBs_0h-incubation and the A431+2D-MNBs_3h-incubation samples were exposed to MH treatment either immediately after the addition of the 2D-MNBs or after 3h of incubation at 37°. After reseeding the cells, the viability was estimated by means of trypan blue assay at well-defined time points (24 or 48 h) post MH-treatment, and it showed severe toxicity for the A431+2D-MNBs_3h sample rather than for the A431+2D-MNBs_0h-incubation sample (Figure 6c). This data support the ac measurements indicating that the disassembling of the 2D-MNBs occurring during the incubation for 3 h at 37 °C produced more cellular heat damages than the A431+2D-MNBs-0h incubation that was not kept at 37 °C for 3 h. The difference is also reflected in the temperature increase that was recorded during the MH treatment: the temperature reached during MH by the A431+2D-MNBs_3h-incubation sample was slightly higher than that of the A431+2D-MNBs_0h-

incubation sample (Figure S9). It should also be noted that the cytotoxicity for the same samples that were not exposed to MH treatment is negligible, independent from the enzymatic incubation. These latter data suggest that the 2D-MNBs and the product of the digestions, that is, the short chains are biocompatible.

Because the 2D-MNBs are composed of several NCs, it was interesting to characterize the behavior of these structures in the presence of a magnet. As macroscopical evidence, we first recorded the time required for a well dispersed suspension of each of the three structures (single NCs, 2D-MNBs, and 3D-MNBs, each of which had the same initial iron amount of 40 μg_{Fe}) to be attracted by a permanent magnet (0.3 T). As was indicated by the transformation of brown liquid to colorless, the 2D-MNBs were very quickly attracted to the magnet (within 80 s, see the panel in Figure 7a2). This response is comparable to that of 3D-MNBs (120 s), while it was not possible to collect any of the single NCs even after 24 h. A quick magnetic response is required to elicit magnetic targeting of materials at the specific target site. Importantly, after magnetic accumulation, both the 2D-MNBs and the 3D-MNBs could be easily resuspended by simply shaking them, which indicates their superparamagnetic behavior at room temperature.

To confirm the magnetic attraction potential at the microscopic scale, we next conducted magnetophoretic mobility experiments with 2D-MNBs, 3D-MNBs, and single NCs. Figure 7b (indexes 1, 2, and 3) show the accumulation on a magnetic nickel rod (50 μm in diameter) magnetized by a 0.2 T magnetic field of NCs and 2D- and 3D-MNBs, respectively. The magnetized rod creates a magnetic field gradient in its surrounding and traps in return magnetic nano-objects according to their magnetic properties. The covering of the magnetic tip thus directly mirrors the magnetic targeting abilities of nano-objects. It clearly appears that nanobeads only (2D or 3D irrespectively) are attracted, the tip being totally uncovered for single NCs, thus confirming the macroscopic magnetic accumulation observed in Figure 7a2. Besides, the migration of the nano-objects toward the tip can be video-monitored to infer the magnetic velocity generated in response to the magnetic field gradient (200 mT/mm in the zone analyzed). Figure 7c1,2 shows typical nanobead magnetic migration. The velocity (μm/s) was then computed for 100 nanobeads for each experiment with the corresponding velocity histograms shown in Figure 7d1,2. The magnetophoretic velocity of 2D-MNBs was derived as 23.6 ± 2.5 μm/s, which was slightly lower than the value that was measured for 3D-MNBs (34.2 ± 1.9 μm/s). It is important mentioning that the hydrodynamic diameter of the 2D-MNBs is far higher (d_H = 393 nm) than the 3D-MNBs (d_H = 171 nm), so that 2D MNBs face a higher viscosity drag friction which restrict their motion. Furthermore, if one estimates the magnetic moments of the clusters from the Stokes equation (see the Materials and Methods section, eq 1), the 2D-MNB moment (m = 4.4 ± 0.4 × 10^{-13} emu) is higher than that of 3D-MNBs (m = 2.7 ± 0.2 × 10^{-13} emu). It could suggest that the planar arrangements of NCs in 2D increases the magnetic moment. However, these values must be taken with care, as the Stokes equation is based on a spherical model, which does not fit the 2D-MNBs, which are more bidimensional assembly. However, it is also important to emphasize that the DLS determination of the hydrodynamic size used in Stokes formula is based on spheres, so that both approximations should compensate.

◼ CONCLUSIONS

In this work, we describe a method for synthesizing bidimensional structures of IONCs by using a low-molecular weight derivative of mcl-PHA, a bacteria-derived, esterase-sensitive biopolymer, as an encapsulating agent. PHA with low-molecular weight enabled self-assembling of the IONCs into a well-defined bidimensional structure. We made a systematic comparison of 2D-MNBs with single NCs and 3D-MNBs produced from the same batch of IONCs. In water, 2D-MNBs exhibited SAR values lower than those of single NCs but two-fold higher than 3D-MNBs. This behavior can be explained due to 2D spatial confinement of IONCs, resulting in special magnetic properties. Such spatial arrangement is weakly influenced by interparticle magnetic dipolar interactions, contrary to 3D-MNBs. Unlike the other two forms, ac hysteresis loops of 2D-MNBs at given frequencies remained almost unaltered even after intentionally inducing their aggregation. Moreover, owing to their high volume to surface ratio, they exhibited a relatively quick response to an external magnet (0.3 T), a crucial property for magnet-guided localization and MH experiments in order to maintain optimal concentrations at the tumor site. Above all, for the first time, we demonstrated an esterase-mediated cleavage of 2D-MNBs into short-chain-like morphologies, when incubated at physiological temperature. Interestingly, because of these evolved structures, it was demonstrated that the SAR value, as a function of the incubation time (up to certain point), almost doubled. In vitro cellular experiments on the A431 cells that were incubated with 2D-MNBs in the presence of esterase demonstrated cellular heat losses and significant cytotoxicity after 3 h of incubation at 37 °C and exposure to MH treatments. This is attributed to the better heating abilities of 2D-MNBs upon esterase disassembling. It is worth to highlight that the enzymatic digestion of 2D-MNBs in the test tube and the in vitro cellular experiment represents a first proof of concept of the action of the esterase enzyme on the 2D-MNBs, leading to the disassembly of chain-like structures, which, in turn, produce more cytotoxic effects on tumor cells than the initial 2D-MNBs under MH. However, for a practical in vivo translation, under lytic enzyme conditions on a real tumor mass, the experimental conditions must be further investigated.[72,73]

Overall, our observations clearly show the potentiality of the 2D-MNBs as MH agents because the heating performance is enhanced via the intracellular enzyme esterase, using the same doses of initial material injected. This could solve the issue of massive decrease in SAR that efficient nanomaterials for MH generally face when internalized and confined within the endosomal intracellular compartment. The results shown here suggest that polymers based on cleavable enzymes could help to design a new generation of IONC-based clusters having dissembling features. This will help to pass from clusters being able to be promptly manipulated under external magnetic fields to intermediate configurations having more performing heating losses and at the same time facilitating their disassembly into smaller portions easy to be degraded and eliminated by the body.

ASSOCIATED CONTENT

ⓈSupporting Information

The Supporting Information is available free of charge on the ACS Publications website at DOI: 10.1021/acs.chemmater.9b00728.

Additional data for the characterization of the PHA polymer (gas chromatogram, mass spectra, and NMR) and for the magnetic materials including TEM images and digital photos of the samples obtained in control experiments elucidating the 2D-MNBs clustering formation, additional DLS characterization of the water-soluble samples, and additional SAR data measured by ac magnetometry on the samples or on the cells treated with the materials and temperature variation recorded by calorimetric measurements on the cells treated with the materials (PDF)

Tomogram and the 3D model of the 2D assembly (MP4)

AUTHOR INFORMATION

Corresponding Author

* E-mail: teresa.pellegrino@it.it.

ORCID ⓘ

Claire Wilhelm: 0000-0001-7024-9627
Francisco J. Teran: 0000-0002-2466-6208
Teresa Pellegrino: 0000-0001-5518-1134

Author Contributions

¶S.K.A. and M.E.M. have contributed equally to this work.

Notes

The authors declare no competing financial interest.

ACKNOWLEDGMENTS

REFERENCES

(1) Abenojar, E. C.; Wickramasinghe, S.; Bas-Concepcion, J.; Samia, A. C. S. Structural effects on the magnetic hyperthermia properties of iron oxide nanoparticles. *Prog. Nat. Sci.: Mater. Int.* **2016**, *26*, 440–448.

(2) Maier-Hauff, K.; et al. Efficacy and safety of intratumoral thermotherapy using magnetic iron-oxide nanoparticles combined with external beam radiotherapy on patients with recurrent glioblastoma multiforme. *J. Neuro-Oncol.* **2011**, *103*, 317–324.

(3) Espinosa, A.; et al. Magnetic (Hyper)Thermia or Photothermia? Progressive Comparison of Iron Oxide and Gold Nanoparticles Heating in Water, in Cells, and In Vivo. *Adv. Funct. Mater.* **2018**, *28*, 1803660.

(4) Cabrera, D.; et al. Dynamical Magnetic Response of Iron Oxide Nanoparticles Inside Live Cells. *ACS Nano* **2018**, *12*, 2741–2752.

(5) Plan Sangnier, A.; et al. Targeted thermal therapy with genetically engineered magnetite magnetosomes@RGD: Photo-

thermia is far more efficient than magnetic hyperthermia. *J. Controlled Release* **2018**, *279*, 271–281.

(6) Silva, A. C.; et al. Application of hyperthermia induced by superparamagnetic iron oxide nanoparticles in glioma treatment. *Int. J. Nanomed.* **2011**, *6*, 591–603.

(7) Lee, J.-H.; et al. Exchange-coupled magnetic nanoparticles for efficient heat induction. *Nat. Nanotechnol.* **2011**, *6*, 418–422.

(8) Bae, K. H.; et al. Chitosan oligosaccharide-stabilized ferrimagnetic iron oxide nanocubes for magnetically modulated cancer hyperthermia. *ACS Nano* **2012**, *6*, 5266–5273.

(9) Guardia, P.; et al. Water-soluble iron oxide nanocubes with high values of specific absorption rate for cancer cell hyperthermia treatment. *ACS Nano* **2012**, *6*, 3080–3091.

(10) Kolosnjaj-Tabi, J.; et al. Heat-Generating Iron Oxide Nanocubes: Subtle "Destructurators" of the Tumoral Microenvironment. *ACS Nano* **2014**, *8*, 4268–4283.

(11) Toulemon, D.; et al. Enhanced Collective Magnetic Properties Induced by the Controlled Assembly of Iron Oxide Nanoparticles in Chains. *Adv. Funct. Mater.* **2016**, *26*, 2454–2462.

(12) Martinez-Boubeta, C.; et al. Learning from nature to improve the heat generation of iron-oxide nanoparticles for magnetic hyperthermia applications. *Sci. Rep.* **2013**, *3*, 1652.

(13) Fu, R.; Yan, Y. Y.; Roberts, C. Study of the effect of dipole interactions on hyperthermia heating the cluster composed of superparamagnetic nanoparticles. *AIP Adv.* **2015**, *5*, 127232.

(14) Corr, S. A.; et al. Linear assemblies of magnetic nanoparticles as MRI contrast agents. *J. Am. Chem. Soc.* **2008**, *130*, 4214–4215.

(15) Mammeri, F.; et al. Formation of Ferrimagnetic Films with Functionalized Magnetite Nanoparticles Using the Langmuir—Blodgett Technique. *J. Phys. Chem. B* **2009**, *113*, 734–738.

(16) Myrovali, E.; et al. Arrangement at the nanoscale: Effect on magnetic particle hyperthermia. *Sci. Rep.* **2016**, *6*, 37934.

(17) Lee, Y.; Lee, H.; Messersmith, P. B.; Park, T. G. A bioinspired polymeric template for 1D assembly of metallic nanoparticles, semiconductor quantum dots, and magnetic nanoparticles. *Macromol. Rapid Commun.* **2010**, *31*, 2109–2114.

(18) Serantes, D.; et al. Multiplying magnetic hyperthermia response by nanoparticle assembling. *J. Phys. Chem. C* **2014**, *118*, 5927–5934.

(19) Materia, M. E.; et al. Mesoscale assemblies of iron oxide nanocubes as heat mediators and image contrast agents. *Langmuir* **2015**, *31*, 808–816.

(20) Ovejero, J. G.; et al. Effects of inter- and intra-aggregate magnetic dipolar interactions on the magnetic heating efficiency of iron oxide nanoparticles. *Phys. Chem. Chem. Phys.* **2016**, *18*, 10954–10963.

(21) Niculaes, D.; et al. Asymmetric Assembling of Iron Oxide Nanocubes for Improving Magnetic Hyperthermia Performance. *ACS Nano* **2017**, *11*, 12121–12133.

(22) Fu, R.; Yan, Y.; Roberts, C.; Liu, Z.; Chen, Y. The role of dipole interactions in hyperthermia heating colloidal clusters of densely-packed superparamagnetic nanoparticles. *Sci. Rep.* **2018**, *8*, 4704.

(23) Andreu, I.; Natividad, E.; Solozábal, L.; Roubeau, O. Nano-objects for addressing the control of nanoparticle arrangement and performance in magnetic hyperthermia. *ACS Nano* **2015**, *9*, 1408–1419.

(24) Bigall, N. C.; et al. Colloidal Ordered Assemblies in a Polymer Shell-A Novel Type of Magnetic Nanobeads for Theranostic Applications. *Chem. Mater.* **2013**, *25*, 1055–1062.

(25) Ortgies, D. H.; et al. Optomagnetic Nanoplatforms for In Situ Controlled Hyperthermia. *Adv. Funct. Mater.* **2018**, *28*, 1704434.

(26) Acharya, S.; Hill, J. P.; Ariga, K. Soft langmuir-blodgett technique for hard nanomaterials. *Adv. Mater.* **2009**, *21*, 2959–2981.

(27) Pauly, M.; et al. Size dependent dipolar interactions in iron oxide nanoparticle monolayer and multilayer Langmuir-Blodgett films. *J. Mater. Chem.* **2012**, *22*, 6343–6350.

(28) Bellido, E.; Domingo, N.; Ojea-Jiménez, I.; Ruiz-Molina, D. Structuration and integration of magnetic nanoparticles on surfaces and devices. *Small* **2012**, *8*, 1465–1491.

(29) Ahniyaz, A.; Sakamoto, Y.; Bergstrom, L. Magnetic field-induced assembly of oriented superlattices from maghemite nanocubes. *Proc. Natl. Acad. Sci. U.S.A.* **2007**, *104*, 17570−17574.

(30) Toulemon, D.; et al. Enhanced Collective Magnetic Properties in 2D Monolayers of Iron Oxide Nanoparticles Favored by Local Order and Local 1D Shape Anisotropy. *Langmuir* **2016**, *32*, 1621−1628.

(31) Pichon, B. P.; et al. 2D assembling of magnetic iron oxide nanoparticles promoted by SAMs used as well-addressed surfaces. *J. Phys. Chem. C* **2010**, *114*, 9041−9048.

(32) Singamaneni, S.; Bliznyuk, V. N.; Binek, C.; Tsymbal, E. Y. Magnetic nanoparticles: Recent advances in synthesis, self-assembly and applications. *J. Mater. Chem.* **2011**, *21*, 16819−16845.

(33) Srivastava, S.; Kotov, N. A. Nanoparticle assembly for 1D and 2D ordered structures. *Soft Matter* **2009**, *5*, 1146−1156.

(34) Zhang, J.; Liu, Y.; Ke, Y.; Yan, H. Periodic square-like gold nanoparticle arrays templated by self-assembled 2D DNA Nanogrids on a surface. *Nano Lett* **2006**, *6*, 248−251.

(35) Guardia, P.; et al. One pot synthesis of monodisperse water soluble iron oxide nanocrystals with high values of the specific absorption rate. *J. Mater. Chem. B* **2014**, *2*, 4426.

(36) Liotta, L. A.; Kohn, E. C. The microenvironment of the tumour-host interface. *Nature* **2001**, *411*, 375−379.

(37) Kaur, G. Strategies for Large-scale Production of Polyhydroxyalkanoates. *Chem. Biochem. Eng. Q.* **2015**, *29*, 157−172.

(38) Rai, R.; Keshavarz, T.; Roether, J. A.; Boccaccini, A. R.; Roy, I. Medium chain length polyhydroxyalkanoates, promising new biomedical materials for the future. *Mater. Sci. Eng., R* **2011**, *72*, 29−47.

(39) Alejandra, R.-C.; Margarita, C.-M.; María Soledad, M.-C. Enzymatic degradation of poly(3-hydroxybutyrate) by a commercial lipase. *Polym. Degrad. Stab.* **2012**, *97*, 2473−2476.

(40) Kaihara, S.; et al. Enzymatic transformation of bacterial polyhydroxyalkanoates into repolymerizable oligomers directed towards chemical recycling. *Macromol. Biosci.* **2005**, *5*, 644−652.

(41) Chen, G.-Q.; Wu, Q. The application of polyhydroxyalkanoates as tissue engineering materials. *Biomaterials* **2005**, *26*, 6565−6578.

(42) Bagdadi, A. V.; et al. Poly(3-hydroxyoctanoate), a promising new material for cardiac tissue engineering. *J Tissue Eng Regen Med* **2018**, *12*, e495−e512.

(43) Lukasiewicz, B.; et al. Binary polyhydroxyalkanoate systems for soft tissue engineering. *Acta Biomater.* **2018**, *71*, 225−234.

(44) Hazer, B. Amphiphilic poly(3-hydroxy alkanoate)s: Potential candidates for medical applications. *Int. J. Polym. Sci.* **2010**, *2010*, 1−8.

(45) Pouton, C. W.; Akhtar, S. Biosynthetic polyhydroxyalkanoates and their potential in drug delivery. *Adv. Drug Delivery Rev.* **1996**, *18*, 133−162.

(46) Francis, L.; et al. Controlled delivery of gentamicin using poly(3-hydroxybutyrate) microspheres. *Int. J. Mol. Sci.* **2011**, *12*, 4294−4314.

(47) Luef, K. P.; Stelzer, F.; Wiesbrock, F. Poly(hydroxy alkanoate)s in Medical Applications. *Chem. Biochem. Eng. Q.* **2017**, *29*, 287−297.

(48) Li, Z.; Loh, X. J. Water soluble polyhydroxyalkanoates: Future materials for therapeutic applications. *Chem. Soc. Rev.* **2015**, *44*, 2865−2879.

(49) Akaraonye, E.; et al. P(3HB) Based Magnetic Nanocomposites: Smart Materials for Bone Tissue Engineering. *J. Nanomater.* **2016**, *2016*, 1−14.

(50) Rai, R.; et al. Highly elastomeric poly(3-hydroxyoctanoate) based natural polymer composite for enhanced keratinocyte regeneration. *Int. J. Polym. Mater. Polym. Biomater.* **2017**, *66*, 326−335.

(51) Girdhar, A.; Bhatia, M.; Nagpal, S.; Kanampalliwar, A.; Tiwari, A. Process Parameters for Influencing Polyhydroxyalkanoate Producing Bacterial Factories: An Overview. *J. Pet. Environ. Biotechnol.* **2014**, *04*, 155.

(52) Di Corato, R.; et al. Magnetic-fluorescent colloidal nanobeads: Preparation and exploitation in cell separation experiments. *Macromol. Biosci.* **2009**, *9*, 952−958.

(53) Basnett, P.; et al. Biosynthesis and characterization of a novel, biocompatible medium chain length polyhydroxyalkanoate by Pseudomonas mendocina CH50 using coconut oil as the carbon source. *J. Mater. Sci.: Mater. Med.* **2018**, *29*, 179.

(54) Gomes, J.; Grunau, A.; Lawrence, A. K.; Eberl, L.; Gademann, K. Bioinspired, releasable quorum sensing modulators. *Chem. Commun.* **2013**, *49*, 155−157.

(55) Gillich, T.; et al. PEG-stabilized core-shell nanoparticles: Impact of linear versus dendritic polymer shell architecture on colloidal properties and the reversibility of temperature-induced aggregation. *ACS Nano* **2013**, *7*, 316−329.

(56) Kremer, J. R.; Mastronarde, D. N.; McIntosh, J. R. Computer visualization of three-dimensional image data using IMOD. *J. Struct. Biol.* **1996**, *116*, 71−76.

(57) Atkinson, W. J.; Brezovich, I. A.; Chakraborty, D. P. Usable Frequencies in Hyperthermia with Thermal Seeds. *IEEE Trans. Biomed. Eng.* **1984**, *BME-31*, 70−75.

(58) Spirou, S.; Basini, M.; Lascialfari, A.; Sangregorio, C.; Innocenti, C. Magnetic Hyperthermia and Radiation Therapy: Radiobiological Principles and Current Practice. *Nanomaterials* **2018**, *8*, 401.

(59) Connord, V.; Mehdaoui, B.; Tan, R. P.; Carrey, J.; Respaud, M. An air-cooled Litz wire coil for measuring the high frequency hysteresis loops of magnetic samples-A useful setup for magnetic hyperthermia applications. *Rev. Sci. Instrum.* **2014**, *85*, 093904.

(60) Mehdaoui, B.; et al. Influence of a transverse static magnetic field on the magnetic hyperthermia properties and high-frequency hysteresis loops of ferromagnetic FeCo nanoparticles. *Appl. Phys. Lett.* **2012**, *100*, 052403.

(61) Materia, M. E.; et al. Mesoscale assemblies of iron oxide nanocubes as heat mediators and image contrast agents. *Langmuir* **2015**, *31*, 808−816.

(62) Cho, M.; et al. Assembly of Iron Oxide Nanocubes for Enhanced Cancer Hyperthermia and Magnetic Resonance Imaging. *Nanomaterials* **2017**, *7*, 72.

(63) Coral, D. F.; et al. Effect of Nanoclustering and Dipolar Interactions in Heat Generation for Magnetic Hyperthermia. *Langmuir* **2016**, *32*, 1201−1213.

(64) Raza, Z. A.; Riaz, S.; Banat, I. M. Polyhydroxyalkanoates: Properties and chemical modification approaches for their functionalization. *Biotechnol. Prog.* **2018**, *34*, 29−41.

(65) Zhang, N.; et al. From 1D Polymers to 2D Polymers: Preparation of Free-Standing Single-Monomer-Thick Two-Dimensional Conjugated Polymers in Water. *ACS Nano* **2017**, *11*, 7223−7229.

(66) Ovejero, J. G.; et al. Effects of inter- and intra-aggregate magnetic dipolar interactions on the magnetic heating efficiency of iron oxide nanoparticles. *Phys. Chem. Chem. Phys.* **2016**, *18*, 10954−10963.

(67) Di Corato, R.; et al. Magnetic hyperthermia efficiency in the cellular environment for different nanoparticle designs. *Biomaterials* **2014**, *35*, 6400−6411.

(68) Soukup, D.; Moise, S.; Céspedes, E.; Dobson, J.; Telling, N. D. In situ measurement of magnetization relaxation of internalized nanoparticles in live cells. *ACS Nano* **2015**, *9*, 231−240.

(69) Alphandéry, E.; Faure, S.; Seksek, O.; Guyot, F.; Chebbi, I. Chains of Magnetosomes Extracted from AMB-1 Magnetotactic Bacteria for Application in Alternative Magnetic Field Cancer Therapy. *ACS Nano* **2011**, *5*, 6279−6296.

(70) Fu, R.; Yan, Y.; Roberts, C.; Liu, Z.; Chen, Y. The role of dipole interactions in hyperthermia heating colloidal clusters of densely-packed superparamagnetic nanoparticles. *Sci. Rep.* **2018**, *8*, 4704.

(71) Lima, E.; et al. Heat generation in agglomerated ferrite nanoparticles in an alternating magnetic field. *J. Phys. D: Appl. Phys.* **2013**, *46*, 045002.

(72) Dong, H.; Pang, L.; Cong, H.; Shen, Y.; Yu, B. Application and design of esterase-responsive nanoparticles for cancer therapy. *Drug Delivery* **2019**, *26*, 416−432.

(73) McGoldrick, C. A.; et al. Identification of oxidized protein hydrolase as a potential prodrug target in prostate cancer. *BMC Cancer* **2014**, *14*, 77.